

# Optical Near-Field Mapping of Plasmonic Nanoprisms

Matthias Rang,<sup>†,‡,§</sup> Andrew C. Jones,<sup>†,‡</sup> Fei Zhou,<sup>||</sup> Zhi-Yuan Li,<sup>||</sup>  
Benjamin J. Wiley,<sup>‡</sup> Younan Xia,<sup>⊥</sup> and Markus B. Raschke<sup>\*,‡</sup>

*Department of Chemistry and Department of Physics, University of Washington, Seattle, Washington 98195, Forschungsinstitut am Goetheanum, CH 4143 Dornach, Switzerland, Institute of Physics, Chinese Academy of Sciences, Beijing 100080, People's Republic of China, and Department of Biomedical Engineering, Washington University, St. Louis, Missouri 63130*

Received June 23, 2008; Revised Manuscript Received August 7, 2008

## ABSTRACT

The optical local-field enhancement on nanometer length scales provides the basis for plasmonic metal nanostructures to serve as molecular sensors and as nanophotonic devices. However, particle morphology and the associated surface plasmon resonance alone do not uniquely reflect the important details of the local field distribution. Here, we use interferometric homodyne tip-scattering near-field microscopy for plasmonic near-field imaging of crystalline triangular silver nanoprisms. Strong spatial field variation on lengths scales as short as 20 nm are observed sensitively depending on structural details and environment. The poles of the dipole and quadrupole plasmon modes, as identified by phase-sensitive probing and calculations performed in the discrete dipole approximation (DDA), reflect the particle symmetry. Together with the observation that the largest enhancement is not necessarily found to be associated with the tips of the nanoprisms, our results provide critical information for the selection of particle geometries as building blocks for plasmonic device applications.

The development of novel chemical synthetic methods has led to crystalline metal nanoparticles with structural control down to the nanometer range and of sizes and shapes inaccessible by conventional lithographic techniques. This includes cubes,<sup>1</sup> prisms,<sup>2–4</sup> rods,<sup>5</sup> or spheroids<sup>6</sup> of several metals and their alloys which allow for the excitation of surface plasmon polariton (spp) eigenmodes which are often stronger and better defined compared to those of polycrystalline structures produced by electrothermal depositions.<sup>7</sup> Their unique optical properties offer potential for diverse applications such as surface-enhanced Raman<sup>8,9</sup> and fluorescence spectroscopies,<sup>10,11</sup> molecular sensing,<sup>12</sup> biomedical diagnostics,<sup>13,14</sup> tomography agents,<sup>15–17</sup> cancer therapy,<sup>15,18,19</sup> photonic circuits,<sup>20,21</sup> and optical waveguides.<sup>22,23</sup>

Most of these applications rely on the optical near-field distribution and its local enhancement on nanometer length scales. However, the design of structures with specific optical near-field properties has remained difficult. This is due to a lack of suitable selection criteria, as the knowledge alone of the particle morphology and its related spp resonance is

insufficient. The details of the local field distribution are not uniquely reflected in the spectrally broad spp response due to the intrinsic ultrafast electronic dephasing.<sup>24</sup> Fundamentally different near-field distributions can result for different nanoparticles with nominally identical spp spectral responses. The knowledge that can be gained from probing the near-field distribution is thus indispensable for the design of plasmonic nanostructures with desired optical functionality. Of the different geometries, plasmonic nanoprisms have emerged as a prototypical building block for nanoplasmonic applications due to the tunability of the plasmon resonance with size over a broad spectral range,<sup>2,4,25</sup> the anticipated strong local-field enhancement associated with the particle tips,<sup>26,27</sup> and the prospect of pairs of nanoprisms to serve as optical antennas.<sup>28–30</sup>

Here, we use interferometric homodyne tip-scattering scanning near-field optical microscopy (*s*-SNOM) to characterize selected vector field components of the local-field distribution of crystalline triangular silver nanoprisms. With a spatial resolution as high as 15 nm, this allows for mapping of the spp modes and identification of their variation with size of the nanostructure. The transition from simple dipole to quadrupole near-field patterns is observed with increasing particle size. Strong local field variations on length scales as short as 20 nm are observed. However, the largest local field enhancements are not necessarily found to be associated

\* Corresponding author. E-mail: raschke@chem.washington.edu.

† These authors contributed equally to this work.

‡ University of Washington.

§ Forschungsinstitut am Goetheanum.

|| Chinese Academy of Sciences.

⊥ Washington University.

with the tips of the nanoprism. In addition to the sensitive relation of the local near-field distribution with nanoscopic structural details of the Ag prisms and their environment, the dependence on polarization, wave vector orientation, and phase retardation with varying structure size is discussed and compared to calculations performed in the discrete dipole approximation (DDA).

**Experiment and Results.** Triangular nanoprisms with sizes ranging from 50 to 400 nm were synthesized from aqueous solution of silver nitrate ( $\text{AgNO}_3$ ) and poly(vinyl pyrrolidone) (PVP) as discussed previously.<sup>4</sup> This method has shown to produce triangular nanoprisms of controllable size with (111) triangular face and (100) side facets as determined by electron diffraction.<sup>31</sup> The nanoprisms were dispersed on glass substrates and rinsed with deionized water to remove residual PVP. The spp response of the individual nanoprisms has been measured using standard white light dark-field microscopy.

The spectral width of the plasmon resonance in the Rayleigh limit is characterized by a simple Drude relaxation damping and independence of particle shape.<sup>24</sup> In general, for both Ag and Au nanoprisms the dipole resonance broadens and red shifts with increasing particle size as has been established both experimentally<sup>2,4,25</sup> and theoretically.<sup>26,27,32</sup> The excitation of quadrupole and other higher order multipole modes leads to the appearance of additional spectral features at higher energies.<sup>4,25</sup> This is seen in Figure 1 which shows the normalized scattering intensity for a nanoprism of approximate edge length of 200 nm together with three typical SEM images of particles of that size. The clear spectral separation of the dipole and multipole modes and their systematic, near linear frequency shift to lower energies with increasing size allows for the investigation of the near-field distribution associated with these different spp modes by tuning the particle size for a fixed laser excitation frequency.

In order to probe the plasmonic near-field of the Ag nanoparticles, the scattering response of a scanning probe tip penetrating the evanescent near-field of the nanoprism is detected. This approach provides enhanced sensitivity and superior spatial resolution down to  $\sim 15$  nm compared to conventional near-field microscopy.<sup>33–36</sup> Additionally, the projection of the near-field polarization and phase into the far-field of the tip-scattered signal uniquely allows for amplitude and phase sensitive probing of the near field of the nanoparticle by homodyne interferometric detection.<sup>37–40</sup>

The experimental setup as shown schematically in Figure 2 is based on a modified atomic force microscope (AFM, CP-Research, Veeco Inc.) with sample scanning and dynamic force control of the cantilever probe tip. The optical setup is designed for the visible to mid-IR spectral range. For the experiments described here, monochromatic excitation from a HeNe laser ( $\lambda = 632.8$  nm) is used for resonant excitation of the optical spp polarization of individual nanoparticles. In an epi-illumination and -detection geometry a Cassegrain objective (NA = 0.5, working distance = 20 mm,  $f = 13$  mm, angle of incidence =  $70^\circ$  with respect to the surface normal) directs the light onto the tip apex region with

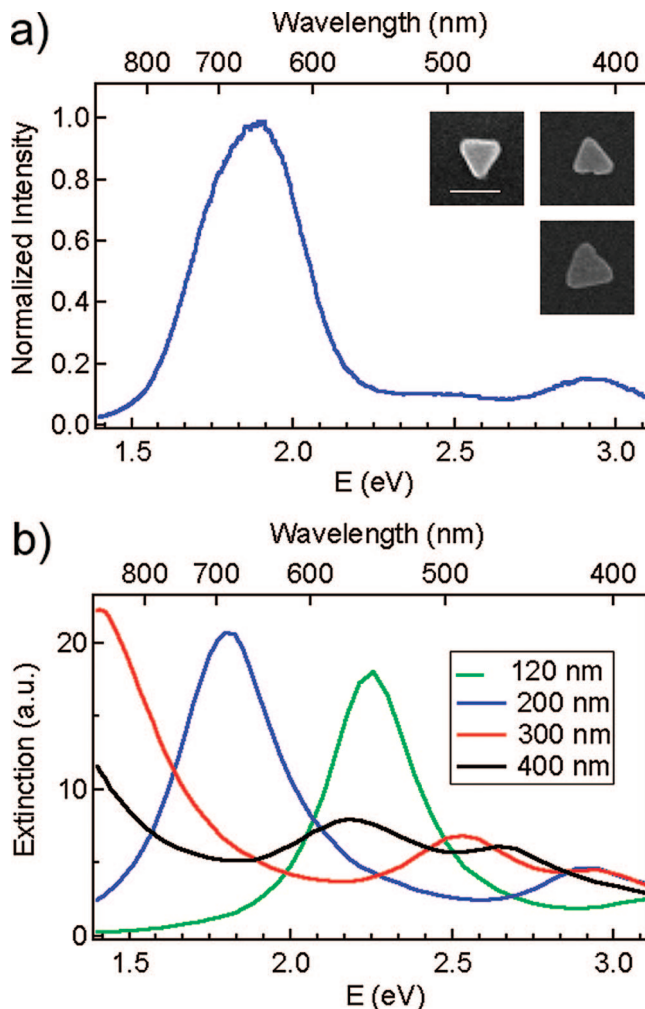


**Figure 1.** Scattering spp spectra of an individual Ag nanoprism (a) of approximate edge length of 200 nm. Inset: representative SEM images of different Ag nanoprisms of corresponding size (scale bar, 200 nm). Calculated optical extinction spectra for Ag nanoprism particles (b) with different sizes (edge length 120, 200, 300, and 400 nm) with truncated tips under s-polarized incident light. The spectra are characterized by a dominant dipole excitation and weaker, spectrally separated multipole modes at higher energies. The resonances systematically shift to lower energies with increasing particle size.

elliptical focus size of  $\sim 2 \mu\text{m}$  in width at a power of  $\sim 5$  mW. The incident and detected polarizations can be controlled by polarizing optics with s and p defined with respect to the plane formed by incidence/emission  $\mathbf{k}$ -vector and the tip axis. For the scattering experiments, individual nanoprisms of desired size are located by AFM scanning. Under laser illumination the tip-scattered near-field response of the particle is then recorded simultaneously with the topography. With the s-SNOM acquisition times between 10 and 60 min, small sample drifts result in image distortions as indicated by the slightly different shapes of the dashed image contours.

Silicon scanning probe tips (ATEC NC-20, Nanosensors) are used as near-field probes. Probing the optical near-field is necessarily associated with a frustration of the evanescent field of the nanostructure. Silicon as a tip material ensures a small perturbation of the intrinsic particle near-field distribution albeit at the expense of a reduced signal intensity

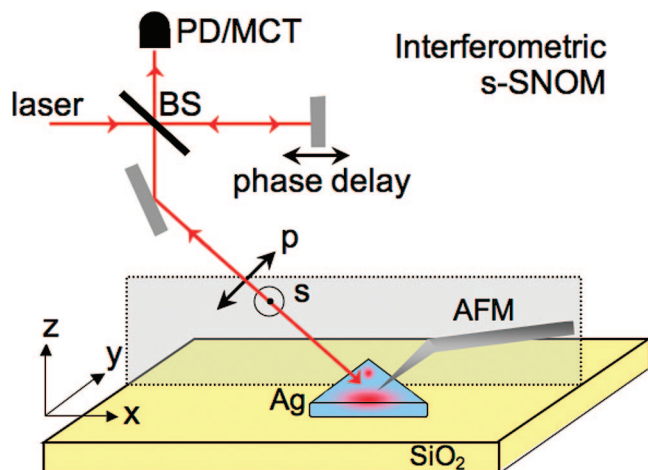


**Figure 2.** Schematic of experimental setup: Polarization selective excitation of silver nanoprisms of different sizes at 632 nm and probing of the evanescent near-field distribution by scattering-type scanning near-field microscopy (s-SNOM). The use of silicon probe tips ensures minimal perturbation of the intrinsic particle near-field distribution. Phase and polarization sensitive information is obtained by interferometric homodyne detection.

compared to the use of metallic probe tips. Due to the lack of antenna or plasmon resonances at visible wavelengths for Si tips, the invasive effect of the probe is minimized especially with regard to the strong plasmon resonant polarization of the crystalline Ag nanoprisms. The tip scatters both s- and p-polarized light effectively;<sup>41</sup> however, the magnitude of the scattering is dependent on the geometry-related tip scattering function.<sup>37,38,42</sup> While the tip scatters both s- and p-polarizations, generally the magnitude of the scattering of the p-component is stronger.

The tip-scattered near-field signal is directed onto a silicon photodiode (model 1801, New Focus). An optional interferometric detection with a reference beam of adjustable phase is used for homodyne amplification in order to extract the near-field phase information (see Appendix). Selection of the polarization of the reference field is performed by use of a  $\lambda/4$  waveplate in the reference arm. The nanoprism near-field response is discriminated from the far-field background by signal demodulation at the second and higher harmonics of the cantilever tip-sample dither frequency by lock-in detection.<sup>43</sup>

Figure 3 shows the resulting near-field pattern obtained for a small rounded Ag prism exhibiting a resonant dipole excitation with an edge length of  $l \approx 120$  nm and a height of  $h \approx 35$  nm for different excitation and detection polarization combinations. Topography (a) and s-SNOM data of the second-harmonic demodulated optical signal (c) are shown for s-polarized resonant excitation and scanning in the xy plane as defined in Figure 2. The corresponding out-of-plane field localization in the z direction is illustrated by a s-SNOM measurement in the yz plane shown in Figure 3b which was performed along the trajectory indicated by the white dashed line in the topography scan.

The observed field localization to within just several tens of nanometers above the nanoparticle confirms the evanescent near-field character of the signal detected in these experi-

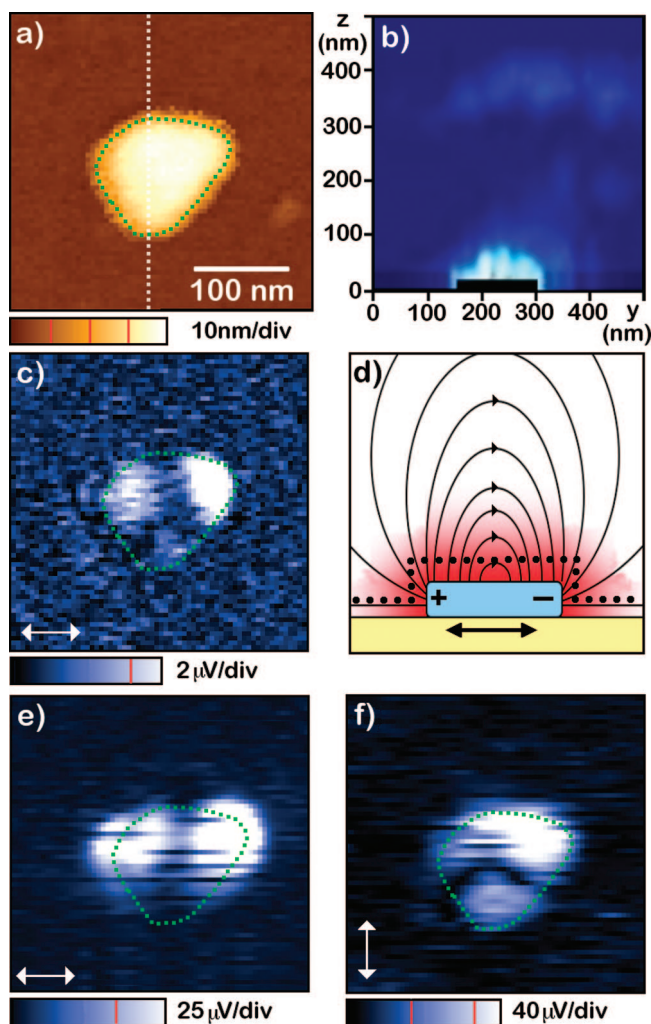


**Figure 3.** Topography (a) and corresponding near-field s-SNOM images for a rounded single crystal Ag nanoprism exhibiting a dipolar excitation. For s-polarized excitation and noninterferometric detection (c) the signal is dominated by the out-of-plane z-component,  $|E_z|$ . The spatial 3D field localization to within tens of nanometers above the particle is seen from the xz scan (b) for p-polarization excitation along the trajectory indicated by the dashed line in the topography (a). For comparison, in homodyne amplification detection in  $s_{inSamp}$  polarization configuration the in-plane field component  $|E_x|$  is probed (e) as compared to  $|E_z|$  for  $p_{inPamp}$  (f). Schematic (d) shows a corresponding model field distribution with tip scan line indicated (dotted). Arrows indicate incident polarization.

ments. From polarization selective detection, it can be shown that the s-SNOM signal without interferometric detection predominantly probes the out-of-plane  $|E_z|$ -component of the nanoparticle (Figure 3c). For comparison, Figure 3e shows corresponding s-SNOM results of the same particle applying interferometric homodyne signal amplification for s-polarized excitation and s-polarized detection ( $s_{inSamp}$ ), amplifying the in-plane  $|E_x|$  field distribution. Similarly, for p-polarized excitation and detection ( $p_{inPamp}$ ) as shown in Figure 3f the  $|E_z|$  component is probed. In contrast to the  $|E_z|$  field, which is predominantly concentrated at the near-edge regions confined within the boundaries of the particle (Figure 3c,f), the in-plane  $|E_x|$  field exhibits significant intensity beyond the outer periphery of the nanostructure (Figure 3e) consistent

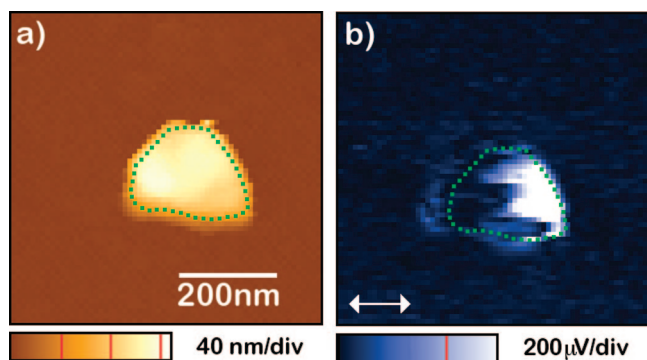


**Figure 4.** Topography (a) and phase-sensitive homodyne detection of  $|E_z|$  for resonant dipole excitation at  $\lambda = 633$  nm with a relative reference phase  $\Phi_{\text{ref}} = \pi$  (b) leading to destructive interference (left) and constructive amplification (right) of the different phase regions of the dipolar near-field.

with the expected dipolar field distribution as shown schematically in Figure 3d.

For dipole excitation the  $|E_z|$  field components at opposite ends of the nanoparticle oscillate out of phase with respect to each other by a relative value of  $\phi = \pi$ . Figure 4 shows phase sensitive near-field imaging by interferometric homodyne detection of a small Ag prism under *s*-polarized excitation. In this case, homodyne amplification of the *p*-polarized component of the scattered light leads to constructive amplification of the right lobe and destructive interference of the left lobe in the *s*-SNOM scan, thus identifying the poles and the dipole character of the excitation.

Full spatial characterization of a specific electric vector field component, which must include measurement of both magnitude and phase,<sup>37</sup> has previously been demonstrated using *s*-SNOM with pseudoheterodyne detection methods.<sup>40</sup> For simple geometries, homodyne amplification, which does not specifically measure the optical phase but allows for preferential phase sensitive amplification of a specified phase region, can reveal the nature of the resonant excitation through its easily interpretable spatial field distribution. For complex geometries, measurement of the magnitude and phase of each electric field component for each 3D spatial coordinate would be required to fully characterize the nature of the excitation.

Figure 5 shows corresponding *s*-SNOM results for a large particle with an edge length of  $l \approx 450$  nm. For 633 nm excitation wavelength the response is dominated by the quadrupole excitation (Figure 1).<sup>4,27,44</sup> The *s*-SNOM images in Figure 5 are observed for *p*- (c) and *s*-polarized (b) excitation. They exhibit large spatial modulations on length scales as short as 20 nm as seen in the lateral signal cross sections (d, e). The dominant features of the near-field distribution observed can be identified with the quadrupolar *spp* excitation as discussed below.

Numerical calculations using the discrete dipole approximation (DDA)<sup>45</sup> provide insight into the origin of the *spp* mode structure and its variation with particle size. Figure 6 shows calculated near-field patterns expected under the experimental conditions with angle of incidence of  $70^\circ$  and

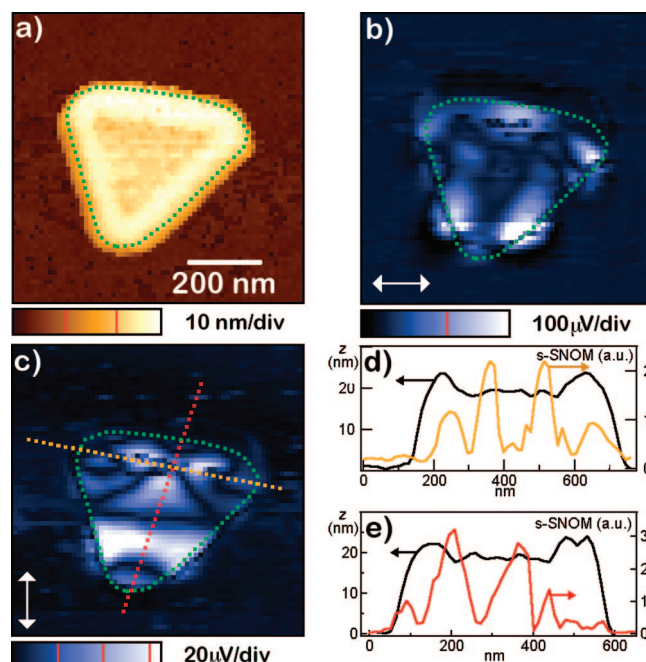


**Figure 5.** Topography (a) and corresponding tip-scattered near-field images at 633 nm for *p*- (c) and *s*-polarization (b), of a large single crystal Ag nanoprism exhibiting quadrupole excitation. The *s*-SNOM cross sections (d, e) indicate spatial field variations at length scales as short as 20 nm.

both polarization excitations for 633 nm light, i.e., with the driving electric field parallel or perpendicular with respect to the top edge of the prism. For the dipole resonance of a small nanoprism with edge length of 120 nm, the calculated near-field patterns 20 nm above the triangular plate surface are displayed for the total field intensity ( $|E^2| = |E_x^2 + E_y^2 + E_z^2|$ ) (a), the *z*-component field intensity ( $|E_z^2|$ ) (b), and the in-plane component field intensity ( $|E_x^2 + E_y^2|$ ) (c). The largest field and strongest confinement at the tips is found for  $E_z$  with the two poles being out of phase in accordance with the experimental observation. The weaker in-plane field exhibits a more extended spatial distribution beyond the particle boundaries (see Figure 3e and Figure 6c). For orthogonal polarization, i.e., driving the plasmon eigenmode between a prism tip and its opposite edge, the enhancement is spatially less confined not only at the edge as expected but also at the prism tip as evident from the  $|E_z|$  field distribution (Figure 3f). This can be rationalized considering the induced free electron current being scattered by the tapering prism edges under an angle with respect to the driving optical laser field.

The calculated near-field patterns for a quadrupole resonance as associated with a large nanoprism particle are shown in Figure 6d–f. Figure 6d represents the distribution of the total field intensity,  $|E^2|$ , under *s*-polarized incidence. Panels e and f of Figure 6 represent the total field  $|E^2|$  and its *z*-component  $|E_z^2|$ , respectively, under *p*-polarized excitation. Similar to the case of small prisms, the *z*-component dominates over the in-plane field. In *p*-polarized excitation, the *spp* near-field pattern shows a quadrupole response characterized by four field enhanced regions (plus and minus signs indicate their relative phases). These poles exhibit

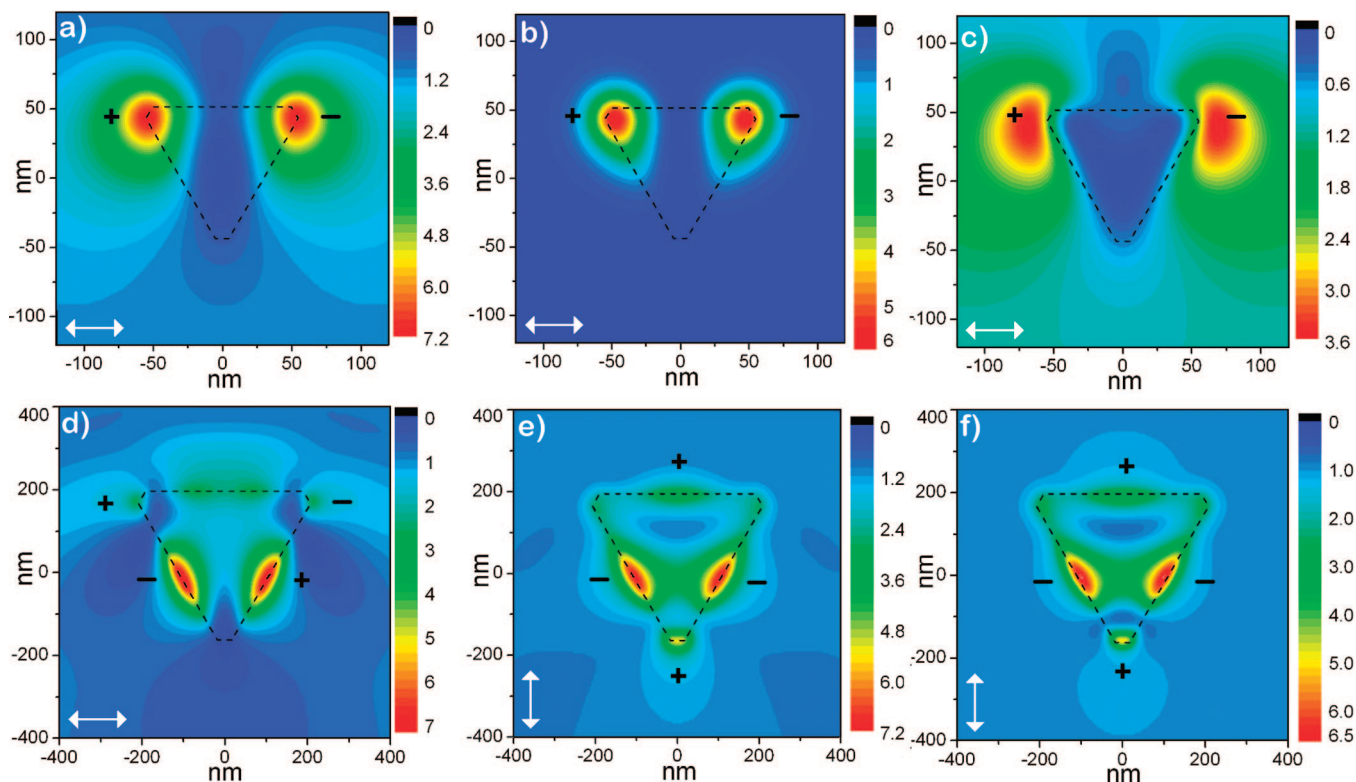


**Figure 6.** Calculated optical near-field distribution of the Ag nanoprism for 633 nm excitation. Top row: dipolar mode for nanoprism with edge length 120 nm, thickness 35 nm, and 10 nm truncated from each tip under *s*-polarized excitation, with total field  $|E^2| = |E_x^2 + E_y^2 + E_z^2|$  (a), *z*-component  $|E_z^2|$  (b), and in-plane field  $|E^2| = |E_x^2 + E_y^2|$  (c). Bottom row: quadrupolar fields of nanoprism with edge length 450 nm, thickness 25 nm, and 35 nm truncated from each tip. Panel d shows the total field  $|E^2|$  under the *s*-polarized excitation. Panels e and f represent the total field  $|E^2|$  and *z*-component  $|E_z^2|$  under *p*-polarized illumination, respectively. Signs represent relative phase of quadrupoles.

unequal field intensity and different shape as also observed in the experiment. In accordance with experiment both *s*- and *p*-polarization give rise to a large local field enhancement at the lower two adjacent edges which dominates over the corresponding fields found at the tips (Figure 5b,c). For *s*-polarization, the other two weaker charge centers of the quadrupole can be discerned at the two tips located at either end of the top edge of the prism as seen in Figure 5b (experiment) and Figure 6d (theory). Similarly, for the *p*-polarized case only one pole is located at a tip giving rise to a corresponding small field enhancement for the lower tip as seen in Figure 5, panel c, (experiment) and Figure 6, panels e and f (theory). With an oblique angle of incidence and structure sizes up to several hundred nanometers, phase retardation can influence the spp excitation. However, varying the angle of incident radiation, comparison of further calculations (data not shown) with the results shown in Figure 6 indicates that retardation of the excitation field has minimal effects on the quadrupolar modal distribution observed.

In agreement with the experimental observation, the calculations also predict the additional polarization density along the top edge of the prism. The quadrupole assignment for *s*-polarized excitation is furthermore consistent with the theoretically derived quadrupole vector field in ref 27. The interference of the quadrupole mode with dipole and higher order modes may give rise to the additional signal modulations at higher spatial frequencies as observed in the

experiments together with possible effects due to deviations from the ideal equilateral triangular shape and inhomogeneities in the illumination.

Observed optical signals between separate scans of *s*- and *p*-polarization in Figures 3 and 5 differ by less than a factor of 2, which is a good indication that the fields induced by each polarization excitation are of comparable strength as indicated by numerical simulations in Figure 6. It should be noted however, that a quantitative comparison of the relative strength of the different polarization components of *s*-SNOM fields is difficult in general. Even with reference homodyne amplification, a polarization anisotropic self-homodyning background of unspecified phase from the far field and tip scattering may still affect the magnitude of the detected signal.

**Discussion.** The nature of the multipolar excitations has been of interest since the first experimental observations of spectral features at higher optical frequencies in Au or Ag nanoprisms.<sup>3,27,46</sup> Here, our results provide the first identification of the corresponding near-field distribution with ultrahigh spatial resolution. The reduced dimensionality, resultant from the high aspect ratio in terms of edge length with respect to thickness, uniquely allows for the suppression of out-of-plane modes and the spectral separation of quadrupole and even higher order mode excitation for these effectively 2D structures.<sup>27</sup> This behavior is akin to elongated quasi-1D rods<sup>47</sup> where spectrally well-separated multipole resonances

can be observed. This is in contrast to, e.g., spherical particles, where the multipolar resonances are not spectrally distinct from the broadening of the dipolar resonance.

It was noted theoretically that the multimode excitation in plasmonic nanoprisms becomes increasingly efficient with increasing size and decreasing thickness giving rise to a surprisingly strong surface plasmon polarization density across large areas of the nanoprism.<sup>27</sup> Our experiments seem to confirm this prediction: The tip-scattered intensities of the multipole modes for large prisms are comparable to the signal obtained for the small dipolar nanoprisms under otherwise identical experimental conditions. This behavior can be interpreted with the prism thickness being comparable to or thinner than the skin depth of  $\sim 30$  nm for Ag at the excitation wavelength of 633 nm. As a result, the optical field inside the prism experiences a low loss of the multimode field excitations that are otherwise strongly damped in the bulk due to the smaller wavevectors associated with them.<sup>27</sup> Note however, that the near-field intensities are not necessarily reflected in intense radiative far-field emission as seen by the comparably small scattering intensities of the multipoles. This is due to the in general larger wavevector mismatch of the multipole vs the dipole excitation with the optical far-field as known from antenna theory.<sup>47</sup>

Contrary to intuitive expectation, in cases of multipole excitation as seen in the data presented here and other data for different sized prisms (data not shown), the tips of the triangles in general do not represent regions of highest local field enhancement. While higher order modes are expected to penetrate more effectively into smaller geometrically confined regions due to their larger wavevector,<sup>44</sup> these regions are not necessarily associated with the highest polarization density.

Eigenmodes complementary to the optical spp have recently been studied in small Ag nanoprisms using electron energy loss spectroscopy (EELS) microscopy.<sup>48</sup> Direct correlation between EELS and the photonic local density of states (LDOS) has been demonstrated in thin film and semi-infinite geometries.<sup>49</sup> In terms of the characterization of metallic nanostructures, while EELS is able to provide information related to the LDOS with nanometer precision, it does not provide a direct measurement of the field associated with SPP resonance.

In summary, our experiments reveal for the first time the microscopic local field distribution associated with characteristic spp dipole and quadrupole modes of crystalline plasmonic Ag nanoprisms. With a spatial resolution as high as  $\sim 15$  nm, an unexpectedly rich spatial field modulation is observed for both dipole and quadrupole excitations that is not uniquely reflected in the spectral spp response of the nanoprism. This is the result of the complex eigenmodes associated with the partially broken symmetry of the nanoprism.

The sensitivity of the near-field response with respect to small geometric details emphasizes the high degree of structural control and the necessity for the understanding of the near-field distribution of plasmonic nanostructures for their use in, e.g., Raman and fluorescence spectroscopies or

as optical antenna and waveguide elements for nanophotonic applications.

**Acknowledgment.** The authors thank Mark Achermann, University of Massachusetts, for valuable discussions. Funding from the National Science Foundation (NSF CAREER Grant CHE 0748226 and DMR-0451788) is greatly acknowledged as is support under a National Science Foundation Graduate Research Fellowship. Z.Y.L. thanks the National Natural Science Foundation of China for financial support under 10525419 and 60736041.

**Appendix.** Phase sensitive near-field imaging is achieved by interferometric homodyne detection, combining the tip-scattered near-field signal for each Cartesian field component  $\mathbf{E}_{\text{nf}} = \sum_i \mathbf{E}_{\text{nf},i} e^{i\Phi_{\text{nf},i}t}$  (with  $i = x, y,$  and  $z$ ) with the reference field  $\mathbf{E}_{\text{ref}} = \sum_i \mathbf{E}_{\text{ref},i} e^{i\Phi_{\text{ref},i}t}$  of adjustable amplitude, polarization, and phase.<sup>50</sup> The detected intensity  $I$  for a specific polarization combination is then given by  $I = (\mathbf{E}_{\text{nf}} + \mathbf{E}_{\text{ref}})(\mathbf{E}_{\text{nf}} + \mathbf{E}_{\text{ref}})^* = |\mathbf{E}_{\text{nf}}|^2 + |\mathbf{E}_{\text{ref}}|^2 + 2|\mathbf{E}_{\text{nf}} \cdot \mathbf{E}_{\text{ref}}| \cos \Phi$ , with  $\Phi$  representing the effective phase difference for said polarization,  $\Phi = \Phi_{\text{nf}} - \Phi_{\text{ref}}$ . With  $\mathbf{E}_{\text{nf}}$  exhibiting a tip-sample distance dependence and thus temporal modulation with the tip dither frequency, lock-in detection selects for signal contributions depending on  $\mathbf{E}_{\text{nf}}$  only. Depending on the phase of the reference field this leads to destructive interference or constructive amplification of the near-field  $s$ -SNOM signal of distinct phases from the different regions of the plasmonic particle. For  $s$ -SNOM probing a strongly resonant enhanced plasmonic near-field excitation, in this discussion we neglect tip and sample scattered far-field contributions and the resulting self-homodyne signal offsets. The full details of the phase contrast imaging depend on the intensity of the reference field and the functional form of the distance dependence of  $E_{\text{nf}}(z)$  as will be discussed in detail elsewhere.

**Supporting Information Available:** Corresponding dielectric contrast imaging. This material is available free of charge via the Internet at <http://pubs.acs.org>.

## References

- (1) Sun, Y.; Xia, Y. *Science* **2002**, *298*, 2176–2179.
- (2) Jin, R.; Cao, Y.; Hao, E.; Metraux, G.; Schatz, G.; Mirkin, C. *Nature* **2003**, *425*, 487–490.
- (3) Chen, S.; Carroll, D. *Nano Lett.* **2002**, *2*, 1003–1007.
- (4) Washio, J.; Xiong, Y.; Xia, Y. *Adv. Mater.* **2006**, *18*, 1745–1749.
- (5) Sau, T.; Murphy, C. *Langmuir* **2004**, *20*, 6414–6420.
- (6) Wang, H.; Brandl, D.; Nordlander, P.; Halas, N. *Acc. Chem. Res.* **2007**, *40*, 53–62.
- (7) Ditlbacher, H.; Hohenau, A.; Wagner, D.; Kreibig, U.; Rogers, M.; Hofer, F.; Aussenegg, F.; Krenn, J. *Phys. Rev. Lett.* **2005**, *95*, 257403.
- (8) Talley, C.; Jackson, J.; Oubre, C.; Grady, N.; Hollars, C.; Lane, S.; Huser, T.; Nordlander, P.; Halas, N. *Nano Lett.* **2005**, *5*, 1569–1574.
- (9) Cao, Y.; Jin, R.; Mirkin, C. *Science* **2002**, *297*, 1536–1540.
- (10) Chen, Y.; Munechika, K.; Ginger, D. *Nano Lett.* **2007**, *7*, 690–696.
- (11) Tam, F.; Goodrich, G.; Johnson, B.; Halas, N. *Nano Lett.* **2007**, *7*, 496–501.
- (12) McFarland, A.; VanDuyne, R. *Nano Lett.* **2003**, *3*, 1057–1062.
- (13) Haes, A.; Van Duyne, R. *Anal. Bioanal. Chem.* **2004**, *379*, 920–930.
- (14) Stuart, D.; Yuen, J.; Shah, N.; Lyandres, O.; Yonzon, C.; Glucksberg, M.; Walsh, J.; VanDuyne, R. *Anal. Chem.* **2006**, *78*, 7211–7215.
- (15) Chen, J.; Saeki, F.; Wiley, B.; Cang, H.; Cobb, M.; Li, Z.-Y.; Au, L.; Zhang, H.; Kimmey, M.; Li, X.; Xia, Y. *Nano Lett.* **2005**, *5*, 473–477.
- (16) Cang, H.; Sun, T.; Li, Z.-Y.; Chen, J.; Wiley, B. J.; Xia, Y.; Li, X. *Opt. Lett.* **2005**, *30*, 3048–3050.

- (17) Lin, A. W. H.; Lewinski, N. A.; West, J. L.; Halas, N. J.; Drezek, R. A. *J. Biomed. Opt.* **2005**, *10*, 064035.
- (18) O'Neal, D.; Hirsch, L.; Halas, N.; Payne, J.; West, J. *Cancer Lett.* **2004**, *209*, 171–176.
- (19) Gobin, A.; Lee, M.; Halas, N.; James, W.; Drezek, R.; West, J. *Nano Lett.* **2007**, *7*, 1929–1934.
- (20) Ozbay, E. *Science* **2006**, *311*, 189.
- (21) Vasseur, J.; Akjouj, A.; Dobrzynski, L.; Djafari-Rouhani, B.; El Boudouti, E. *Surf. Sci. Rep.* **2004**, *54*, 1–156.
- (22) Smolyaninov, I. I.; Hung, Y.-J.; Davis, C. C. *Appl. Phys. Lett.* **2005**, *87*, 241106.
- (23) Maier, S.; Kik, P.; Atwater, H.; Meltzer, S.; Harel, E.; Koel, B.; Requicha, A. *Nat. Mater.* **2003**, *2*, 229–232.
- (24) Kreibig, U.; Vollmer, M. *Optical Properties of Metal Clusters*; Springer: Berlin, 1995; Vol. 25.
- (25) Sherry, L.; Jin, R.; Mirkin, C.; Schatz, G.; VanDuyne, R. *Nano Lett.* **2006**, *6*, 2060–2065.
- (26) Kelly, K.; Coronado, E.; Zhao, L.; Schatz, G. *J. Phys. Chem. B* **2003**, *107*, 668–677.
- (27) Shuford, K.; Ratner, M.; Schatz, G. *J. Chem. Phys.* **2005**, *123*, 114713.
- (28) Schuck, P.; Fromm, D.; Sundaramurthy, A.; Kino, G.; Moerner, W. *Phys. Rev. Lett.* **2005**, *94*, 017402.
- (29) Cubukcu, E.; Kort, E.; Crozier, K.; Capasso, F. *Appl. Phys. Lett.* **2006**, *89*, 093120.
- (30) Merlein, J.; Kahl, M.; Zuschlag, A.; Sell, A.; Halm, A.; Boneberg, J.; Leiderer, P.; Leitenstorfer, A.; Bratschitsch, R. *Nat. Photonics* **2008**, *2*, 230–233.
- (31) Wang, Z. *J. Phys. Chem. B* **2000**, *104*, 1153–1175.
- (32) Kottmann, J.; Martin, O.; Smith, D.; Schultz, S. *Opt. Express* **2000**, *6*, 213–219.
- (33) Hillenbrand, R.; Taubner, T.; Keilmann, F. *Nature* **2002**, *418*, 159.
- (34) Cvitkovic, A.; Ocelic, N.; Aizpurua, J.; Guckenberger, R.; Hillenbrand, R. *Phys. Rev. Lett.* **2006**, *97*, 060801.
- (35) Raschke, M.; Molina, L.; Elsaesser, T.; Kim, D.; Knoll, W.; Hinrichs, K. *ChemPhysChem* **2005**, *6*, 2197.
- (36) Neacsu, C. C.; Dreyer, J.; Behr, N.; Raschke, M. B. *Phys. Rev. B* **2006**, *73*, 193406.
- (37) (a) Lee, K. G.; Kihm, H. W.; Kihm, J. E.; Choi, W. J.; Kim, H.; Ropers, C.; Park, D. J.; Yoon, Y. C.; Choi, S. B.; Woo, D. H.; Kim, J.; Lee, B.; Park, Q. H.; Lienau, C.; Kim, D. S. *Nat. Photonics* **2007**, *1*, 243–244; (b) Gersen, H.; Novotny, L.; Kuipers, L.; van Hulst, N. F. *Nat. Photonics* **2007**, *1*, 242.
- (38) Lee, K. G.; Kihm, H. W.; Ahn, K. J.; Ahn, J. S.; Suh, Y. D.; Lienau, C.; Kim, D. S. *Opt. Express* **2007**, *15*, 14993–15001.
- (39) Hillenbrand, R.; Keilmann, F.; Hanarp, P.; Sutherland, D. S.; Aizpurua, J. *Appl. Phys. Lett.* **2003**, *83*, 368–370.
- (40) Ocelic, N.; Huber, A.; Hillenbrand, R. *Appl. Phys. Lett.* **2006**, *89*, 101124.
- (41) Note that these conditions for apertureless or scattering-type probing of evanescent near-field distributions contrasts tip-enhanced s-SNOM where a strong mutual tip–sample polarization coupling is desirable and is typically dominated by p-polarized excitation. For corresponding dielectric contrast imaging, see Supporting Information.
- (42) Ossikovski, R.; Nguyen, Q.; Picardi, G. *Phys. Rev. B* **2007**, *75*, 045412.
- (43) Hillenbrand, R.; Keilmann, F. *Philos. Trans. R. Soc. London, Ser. A* **2004**, *362*, 787–805.
- (44) Achermann, M.; Shuford, K. L.; Schatz, G. C.; Dahanayaka, D. H.; Bumm, L. A.; Klimov, V. I. *Opt. Lett.* **2007**, *32*, 2254–2256.
- (45) Draine, B. T.; Flatau, P. J. *J. Opt. Soc. Am. A* **1994**, *11*, 1491.
- (46) Millstone, J.; Park, S.; Shuford, K.; Qin, L.; Schatz, G.; Mirkin, C. *J. Am. Chem. Soc.* **2005**, *127*, 5312–5313.
- (47) Krenn, J. R.; Schider, G.; Rechberger, W.; Lamprecht, B.; Leitner, A.; Aussenegg, F. R.; Weeber, J. C. *Appl. Phys. Lett.* **2000**, *77*, 3379–3381.
- (48) Nelayah, J.; Kociak, M.; Stephan, O.; Garcia de Abajo, F. J.; Tence, M.; Henrard, L.; Taverna, D.; Pastoriza-Santos, I.; Liz-Marzan, L. M.; Colliex, C. *Nat. Phys.* **2007**, *3*, 348–353.
- (49) Garcia de Abajo, F. J.; Kociak, M. *Phys. Rev. Lett.* **2008**, *100*, 106804.
- (50) Gomez, L.; Bachelot, R.; Bouhelier, A.; Wiederrecht, G.; Chang, S.; Gray, S.; Hua, F.; Jeon, S.; Rogers, J.; Casto, M.; Royer, P.; Lerondel, G. *J. Opt. Soc. Am. B* **2006**, *23*, 823.

NL801808B